THE OBSERVATION AND MEASUREMENT OF SUBSTRUCTURES IN CRYSTALS BY X-RAY TECHNIQUES

by S. Weissmann
College of Engineering, Rutgers · The State University, New Brunswick, N. J.

1. INTRODUCTION

It is universally recognized that a great many properties of solids are significantly affected by small changes in the perfect arrangement of atoms of which the solid is composed. Such properties are said to be structure-sensitive. The three most important classes of structure-sensitive properties of crystalline matter are mechanical, electric and magnetic. Thus the strength and plastic properties of metals and many other crystals, the phenomena of crystal growth and recrystallization, the diffuse properties, optical and dielectrical behavior of insulating crystals, photoconductivity, luminescence and the coercive force are typical structure-sensitive properties. Generally, a relatively small number of lattice defects exerts disproportionately large effects on these properties.

It is proposed to discuss in this paper various x-ray methods used for disclosing crystal imperfections and lattice inhomogeneities and to show how these methods can be effectively linked to light and electron microscopic studies. For it is the belief of this author that through the interplay of these methods a detailed, quantitative elucidation of the defect structure can be achieved. Furthermore, it is proposed to show briefly in the manner of an illustrated travelogue highlights of some applications of these methods to problems of scientific and technological importance alike. Because of the limited scope of this paper the reader will be referred to special publications if details concerning the methods, applications and research results are desired.

2. X-RAY BACK-REFLECTION DIVERGENT BEAM METHOD AND STRAIN ANALYSIS

The divergent beam method is principally a precision method for the determination of lattice parameters and anisotropic lattice distortions of single crystals. It yields also information with regard to local lattice misalignment and, if the patterns are properly interpreted, one may even obtain a topographical mapping of lattice misorientations in the crystal with a limiting resolution of about 3'-4' of arc.

As practiced by the author the divergent beam method utilizes a horizontal capillary x-ray tube designed by T. Imura (1). An electron beam originating from an electron gun is focussed by means of electromagnetic lenses onto the tip of a long capillary tube, where a thin metal foil is placed as an x-ray target. By operating the tube at a suitable voltage an x-ray beam with characteristic radiation emerges from the tip of the x-ray tube, exhibiting a divergence of nearly 180°. When this beam impinges on the test crystal which is placed at a distance of 1-3 mm from the tip of the capillary tube, diffraction patterns of the characteristic

(1) T. Imura, Part I, II, III; J. Jap. Inst. of Metals, 16, 10 (1952); Naniwa Univ. Ser. A, 2, 51 (1954); Bull. Univ. of Osaka Prefecture, Ser. A, 5, 1 (1957).

spectrum in transmission as well as in the back-reflection region are obtained (Fig. 1). These patterns are analogous to the well-known Kossel patterns, except that in the case of the capillary x-ray tube the patterns are produced by an x-ray source which is outside instead of inside the specimen. For want of a better name these patterns were termed pseudo-Kossel patterns.

Of particular interest are the back-reflection patterns which can be obtained with much greater ease than the transmission patterns. Only a few minutes' exposure time is required. Figure 2 is a back-reflection pattern of an Al-3.85% Cu crystal solution heat-treated and water-quenched. Each ellipse corresponds to a definite (hkl) set of planes. By measuring the long axis of the ellipses and the specimen-to-film distance, the interatomic distance, d, of the various (hkl) planes can be determined (1). In a new development a quartz crystal, a few microns thick, is used as an internal calibrator. The quartz crystal is placed in front of the test crystal and both patterns, that of quartz and that of the test crystal, are simultaneously recorded. Using the a_o parameter of quartz as an internal standard the d-spacings can be measured with a precision of $\pm 0.02\%$.

Hosokawa, Padawer and Weissmann (2) have recently developed an alternative method achieving nearly the same degree of precision. In this method the pseudo-Kossel patterns are recorded on the same film at different specimen-to-film distances and the diffraction angle θ of the (hkl) reflection is directly determined from the precisely known distances between consecutive film positions. Let β represent the dip angle, that is, the angle between the optical axis of the capillary tube and the normal of the diffracting (hkl) planes, $\alpha = 90 - \theta$, and let m and n be the measured distances of the corresponding points on the elliptical pseudo-Kossel patterns recorded at film positions a_2 and a_1, respectively, as shown in Fig. 1, where $c = a_2 - a_1$; then the following relationship holds:

$$m/c = \tan(\alpha + \beta) \qquad (1)$$

$$n/c = \tan(\alpha - \beta) \qquad (2)$$

From these two equations α and therefore θ and d(hkl) can be determined directly.

Modifications of the interatomic spacings resulting from physical or chemical processes can be well studied by the divergent beam method, and since individual (hkl) reflections are being measured the anisotropic changes in structure can be uniquely determined. For example, the (hkl) and ($\bar{h}$kl) reflections in a cubic structure give rise to two different ellipses and consequently if anisotropic changes in structure occur the d-values of the two reflections may no longer be identical. One may become larger and the other may indeed become smaller (Fig. 3). By measuring the changes of lattice spacings, Δd, of more than six independent (hkl) reflections and referring them to the d values of the original state, strain values, $\frac{\Delta d}{d}$, are obtained which are used as the raw data for a recently developed strain analysis (3). This analysis, carried out with the aid of a computer, gives the strain distribution in terms of three principal strains, namely, the maximum strain

(2) N. Hosokawa, G. Padawer and S. Weissmann, "Precision Measurements by the X-Ray Back-Reflection Divergent Beam Method," (to be published).
(3) T. Imura, S. Weissmann and J. J. Slade, Jr., Acta Cryst. 15, 786 (1962).

ε_1, the intermediate strain ε_2 and the minimum strain ε_3. The magnitude and direction of the principal strains define completely the strain ellipsoid and consequently the strains in any other desired direction can be computed.

2.1 Applications

A. Lattice Distortions in Age-Hardening of Alloys

The strain analysis based on the back-reflection divergent beam method was applied to the study of age-hardening of an Al-3.85% Cu alloy (3). Various modes of quenching and various stages of age-hardening were investigated. The results of the analysis are given in Table I. The maximum strain corresponding to the ageing stage associated with the formation of the Guinier-Preston zones coincided with one of the [100] directions and shifted about 20° when the θ' phase was predominant. The anisotropy of strain distribution was interpreted in terms of a preferred vacancy migration due to thermal and concentration gradients introduced by quenching.

B. Lattice Defects Induced by Neutron Irradiation

Another interesting application of the method was the determination of the strain distribution in thin quartz crystals induced by fast neutron irradiation(4). Major strain differences were found between crystals cut parallel to the basal (00.1) plane (z-cut) and those cut perpendicular to it (x-cut) (Table II). The x-ray results were interpreted in terms of a mechanism of dynamic crowdions involving the formation of clusters of interstitial atoms aligned in specific directions relative to the open screw channels of the quartz structure, and in terms of a thermal spike mechanism giving rise to cluster formation. It was indeed gratifying when subsequent studies of transmission electron microscopy, carried out on the identical specimens after appropriate thinning by etching, disclosed directly the existence of clusters of point defects. Furthermore, it was found that the alignment of the clusters as determined by means of selected area diffraction coincided with the maximum strain direction deduced from the x-ray study (Fig. 4). Good agreement was also found between the average size of defect clusters determined by transmission electron microscopy and that determined by small-angle x-ray scattering (Table III). This study may serve as a good example for illustrating the interplay of x-ray and electron microscopy techniques, which are not competitive but complementary to each other.

C. Plastic Deformation of Solids

Local misorientations of lattice domains show up as discontinuities in the pseudo-Kossel line pattern. Such discontinuities, indicated by arrows, were made more conspicuous in Fig. 5 by employing a multiple exposure technique in which the specimen-to-film distance was slightly varied between exposures. Whereas ductile metals such as f. c. c. aluminum or b. c. c. tantalum deform at room temperature on many slip systems and therefore exhibit broadening and discontinuities for practically all elliptical lines, brittle metals, viz. molybdenum, deform essentially on few or only on a single slip system and therefore show broadening and discon-

(4)S. Weissmann, T. Imura, K. Nakajima and S. E. Wisnewski, "Lattice Defects of Quartz Induced by Fast Neutron Irradiation" (to be published in Proc. of Symposium on Point Defects, Kyoto, 1962, J. Phys. Soc. Japan).

Table I. Principal strains in age-hardened Al-3.85% Cu crystal, water-quenched after solution treatment.

Heat Treatment	Phases Present	Maximum Strain ε_1			Intermediate Strain ε_2			Minimum Strain ε_3		
		Magnitude in %	Direction Number	Direction	Magnitude in %	Direction Number	Direction	Magnitude in %	Direction Number	Direction
205° C for 20 hours	G. P. [I] -trace + G. P. [II]	0.41	n_1 0.05 n_2 1.00 n_3 -0.18	u 0 v 1 w 0	0.18	n_1 0.17 n_2 0.17 n_3 1.00	u 0 v 0 w 1	-0.10	n_1 1.00 n_2 -0.08 n_3 -0.15	u 1 v 0 w 0
Additional annealing at 320° C for 1/2 hr.	θ'	0.47	n_1 0.04 n_2 1.00 n_3 -0.37	u 0 v 3 w I	0.15	n_1 0.15 n_2 0.37 n_3 1.00	u 0 v 1 w 3	-0.03	n_1 1.00 n_2 -0.08 n_3 0.12	u 1 v 0 w 0
Additional annealing at 430° C for 23 hrs.	Matrix + incoherent θ (equilibrium phase)	0.29	n_1 1.00 n_2 -0.18 n_3 -0.13	u 1 v 0 w 0	-0.08	n_1 0.16 n_2 1.00 n_3 -0.09	u 0 v 1 w 0	-0.02	n_1 0.14 n_2 0.06 n_3 1.00	u 0 v 0 w 1

Table II

Effect of Fast Neutron Irradiation on the Principal Strains in Quartz Crystals

Irradiation nvt (Fast)	Natural Quartz Z-Cut	Z-Face Synthetic Z-Cut	Z-Growth Synthetic Z-Cut	Natural Quartz X-Cut	Z-Face Synthetic X-Cut
	* Magnitude % (h k . l)	Magnitude % (h k . l)	Magnitude % (h k . l)	Magnitude % (h k . l)	Magnitude % (h k . l)
1×10^{19}	ϵ_1 = -0.2812 (2 $\bar{1}$. 0) ϵ_2 = +0.2338 (0 0 . 1) ϵ_3 = +0.0703 (0 1 . 0)	+0.6113 (2 $\bar{1}$. 0) -0.0883 (0 0 . 1) -0.0070 (0 0 . 1)	+0.3850 (3 $\bar{1}$. 1) +0.1777 ($\bar{1}$ 2 . 2) -0.0309 (0 0 . 1)	+1.8070 (1 $\bar{1}$. 0) +0.5607 (0 0 . 1) +0.0246 (1 1 . 0)	+1.6809 (2 $\bar{2}$. 1) +0.3694 (1 $\bar{1}$. 2) -0.0579 (2 1 . 0)
3×10^{19}	ϵ_1 = +0.5793 (0 1 . 0) ϵ_2 = +0.3993 (2 0 . $\bar{1}$) ϵ_3 = +0.0654 (0 0 . 1)	+0.6139 (2 $\bar{1}$. 0) +0.3732 (0 1 . 0) -0.1022 (0 0 . 1)	+0.4372 (1 1 . 0) +0.3172 (1 $\bar{1}$. 0) +0.1511 (0 0 . 1)	+1.8219 (2 $\bar{2}$. 1) +0.4143 ($\bar{1}$ 0 . 2) +0.1705 (0 1 . 0)	+0.9083 (1 $\bar{1}$. 0) +0.2870 (2 4 . $\bar{1}$) -0.0742 (0 0 . 1)
6×10^{19}	ϵ_1 = +0.6142 (2 $\bar{1}$. 0) ϵ_2 = +0.3715 (0 1 . 0) ϵ_3 = +0.0235 (0 0 . 1)	+0.6143 (2 $\bar{1}$. 0) +0.3665 (0 1 . 0) -0.0333 (0 0 . 1)	+0.3913 (1 0 . 0) +0.3258 (0 1 . 0) +0.0584 (0 0 . 1)	+0.7935 (1 $\bar{1}$. 3) +0.4520 (2 $\bar{2}$. $\bar{1}$) +0.0207 (2 1 . 0)	+1.1814 (1 $\bar{1}$. $\bar{1}$) +0.3380 (2 $\bar{1}$. 2) -0.1329 (1 2 . 0)
8×10^{19}			ϵ_1 = +0.3166 ($\bar{1}$ 2 . 0) ϵ_2 = +0.1766 (1 0 . 0) ϵ_3 = -0.1534 (0 0 . 1)		

Legend

*ϵ_1 = maximum strain
ϵ_2 = intermediate strain
ϵ_3 = minimum strain

(h k . l) are Miller indices of planes perpendicular to the direction of strain.

TABLE III

Effect of Neutron Irradiation on Size of Interstitial Clusters and Density in Quartz

Type of Crystal	Irradiation nvt	Mean Radius of Cluster, $\bar{r}$, (Small-Angle X-Ray Scattering) cm	Mean Radius of Cluster, $\bar{r}$, cm (Transmission Electron Microscopy, T. E. M.)	Total Volume of Cluster, Nv, per cm^3 (T. E. M.)	Fractional Change in Density $-\frac{\Delta\rho}{\rho}\%$ *
z-cut	1×10^{19}	--	8×10^{-7}	0.008	0.8
	6×10^{19}	12×10^{-7}	21×10^{-7}	0.04	4.2
	8×10^{19}	--	21×10^{-7}	0.093	9.8
	1×10^{20}	9×10^{-7}	11×10^{-7}**	0.098**	10.4
	1.5×10^{20}	--	8×10^{-7}***	0.053***	--
x-cut	6×10^{19}	9×10^{-7}	6×10^{-7}	0.015	1.6

* $-\frac{\Delta\rho}{\rho} = 1.06Nv$

**In addition to isolated clusters a hexagonal network was observed resulting from the interactions of clusters. Size of hexagon $\approx$ 1000Å.

***Extensive network formation.

tinuities for only a few (hkl) reflections, leaving the other (hkl) reflections virtually unaffected. This opens up an exciting possibility of studying the change in strain distribution during the ductile-brittle transition of a metal. Such studies are currently in progress. For initial stages of deformation of metals the strain distribution on all active slip planes can be determined from the principal strains and the increase or decline of strain can be followed as a function of deformation. The strain distribution measurements of this type are made possible either because of an effective build-up of strains taking place at the specimen surface, where dislocations are being prevented from escaping presumably by barriers of oxide layers, or because of the existence of residual strains resulting from the deformation process.

If a binary alloy foil is used as x-ray target the pseudo-Kossel pattern will consist of two sets of lines corresponding to the target material. Consequently, precision lattice parameter measurements can then be carried out not only as a function of wavelength but also as a function of depth penetration. It is also possible to extend the divergent beam method further by carrying out microphotometric measurements of the line profiles followed by a Fourier transform analysis in order to determine particle size and average local strain (5). Such studies are also currently in progress.

3. COMBINATION OF X-RAY DOUBLE-CRYSTAL DIFFRACTOMETER AND X-RAY DIFFRACTION MICROSCOPY

The double-crystal diffractometer is a precision instrument capable of resolving lattice misorientations of a few seconds of arc. It is, therefore, very well suited for the study of the misfit angle of adjacent subgrains and its modifications induced by mechanical stress or annealing.

In this instrument the incident beam falling on the test crystal is first reflected from a monochromatizing crystal and the beam reflected by the rotating test crystal is registered by an electronic radiation detector. Perfect test crystals will reflect over a very narrow range of specimen rotation, while imperfect crystals having a wider spread of lattice misorientation will reflect over an extended range. In the case of crystals possessing subgrains which are brought successively into reflecting position, the reflection curve will exhibit multiple peaks instead of a single peak (6). Such a reflection curve is illustrated in Fig. 6, where the angular separation of $\approx 30'$ between peaks 3 and 9 defines the misfit angle between two adjacent coarse subgrains. It is interesting to note that in this specific case the misorientation of the coarse subgrains is not large enough to be resolved by conventional x-ray techniques. Thus the back-reflection Laue diagram of this crystal exhibits no visible break-up of the spots.

The most characteristic and useful feature of the double-crystal diffractometer method as employed in this laboratory is the combination of electronic radiation detector and supplementary film technique (6). Although the radiation detector is highly sensitive in registering slight variations in x-ray intensities, it is insensitive in discriminating between the location of different lattice domains on the specimen surface which contribute to a registered intensity value. A film

(5)B. E. Warren, Progress in Metal Physics, 8, Ch. 3, 147, Pergamon Press (1959).
(6)J. Intrater and S. Weissmann, Acta Cryst. 7, 729 (1954).

placed in front of the radiation detector, however, functions as a "guiding eye" to the counter and pins down the location of the reflecting lattice domains which give rise to a specific registered intensity value.

The analysis of the reflection curve of Fig. 6 by means of the supplementary film technique is shown in Fig. 7. This figure exhibits the reflection images of the magnesium crystal recorded photographically in front of the radiation detector at discrete rotation positions of the specimen. The corresponding positions are indicated by numbers. The break-up of the reflection images discloses the existence of microscopic subgrains of which the coarse subgrains are composed. By tracing the reflection images to the specimen surface photographically a topographical mapping of the substructure can be achieved by x-ray diffraction microscopy and correlated to the quantitative analysis of the double-crystal diffractometer method (6, 7, 8).

The topographical mapping of lattice inhomogeneities by x-ray diffraction microscopy was first suggested by Berg (9) and later extended by Barrett (10). It is based upon differences in diffracting power from point to point in the specimen to produce contrast and to enhance the topographical detail of the image. In imperfect crystals image intensification is obtained by diffraction from adjacent lattice domains which are curved or misaligned in a concave manner, while diffraction from lattice domains curved or misaligned in a convex manner will give rise to a dispersion of the diffracted beam. In the former case the image will be darker, whereas in the latter case it will be lighter than the background.

Figure 9 shows the instrument with the aid of which the analysis of the magnesium crystal (Figs. 6, 7) was carried out. Not only single crystals but also polycrystalline materials can be analyzed by the combination method. By means of the movable upper platform, which can be rotated around an axis coincident with that of the monochromatizing first crystal, the test specimen can be irradiated successively with unfiltered and crystal-monochromatized radiation (8). In the case of a polycrystalline specimen this technique permits one to trace the reflection curves to the corresponding grains on the specimen surface and to analyze these grains for their substructure characteristics (8).

Depending on the perfection of the grains, the specimen is rotated in angular intervals of seconds or minutes of arc and the spot reflections of the grains, recorded for each discrete specimen rotation, are separated by film shifts. This multiple exposure technique gives rise to an array of spots for each reflecting grain. Since each grain may be regarded as the test crystal of a double-crystal diffractometer, the array of spots is analogous to the reflection (rocking) curve of a single crystal and can be analyzed in a similar manner. Thus, if the grains contain a substructure the intensity distribution of the array of spots shown in Fig. 8 will be multi-peaked in complete analogy to the reflection curves obtained from single crystals containing substructure. In the case of single crystals indi-

(7) S. Weissmann, J. Appl. Phys., 27, 389 (1956).
(8) S. Weissmann, Trans. Am. Soc. for Metals, 52, 599 (1960).
(9) W. Berg, Naturwissenschaften 89, 286 (1934).
(10) C. S. Barrett, Trans. Am. Inst. Min. and Metall. Engrs. 161, 15 (1945).

vidual subgrain boundaries can even be analyzed if an exposure superposition technique is used (11).

3.1 Applications

A. Substructure and Dislocation Networks in Tungsten (11)

The existence of three orders of magnitude of subgrains was disclosed in a single crystal of tungsten produced by the arc fusion method. Two orders of subgrains, namely, the macroscopic and microscopic subgrains--also termed first and second order subgrains--are shown in the reflection micrograph of Fig. 10. This micrograph was taken with unfiltered copper radiation using a microfocussing tube with an effective focal spot size of 40 μ. Both the specimen as well as the fine-grained photographic plate, placed 1 mm from the specimen, were oscillated over a range of $\approx 1^{\circ}$ of arc. Applying the exposure superposition technique shown in Fig. 11, which consists of the successive application of unfiltered and crystal-monochromatized radiation, the individual sub-boundaries such as those separating the macroscopic subgrains A and B were directly analyzed. The reflection curve taken with crystal-monochromatized radiation, shown in Fig. 12, consists of two major peaks, one pertaining to subgrain A and the other to subgrain B. Since the sub-boundary was so oriented that it coincided with the specimen rotation axis, the peak-to-peak separation of 16.5' yielded directly the disorientation angle between the subgrains. From this angle the dislocation density in the sub-boundary was computed to be 8.8×10^5 per cm^2. By employing the supplementary film technique at the rotation positions indicated by numbers in Fig. 12, the microscopic subgrains, marked by the small letters a→f in the corresponding metallograph of Fig. 11a, were analyzed. The disorientation angle of the microscopic subgrains ranged from 1'-4' of arc and the dislocation density in the sub-boundaries from 7.7×10^5 to 2.2×10^6 per cm^2. The smallest subgrains (third order), about 10 μ in size, were directly disclosed by transmission electron microscopy after the specimen was appropriately thinned by electropolishing. The average dislocation density in the sub-boundaries turned out to be 1.8×10^6 per cm^2 (11).

B. Mechanical and Thermal Stability of Low-Angle Boundaries (12)

The mechanical and thermal stability of low-angle boundaries in zinc single crystals were studied by methods combining light microscopy with the x-ray combination method described above. The modifications of the x-ray reflection curves during isothermal annealing were studied by means of a special timing device attached to the reversible motor which controls the rotation of the precision goniometer head holding the test specimen. The time intervals for reversible specimen rotation were controlled by an interchangeable cam system. Consequently, the entire reflection curve or portions of the reflection curve could be repeated as desired during isothermal annealing and the modifications in the x-ray profile could be studied as a function of annealing time. Thus, if no detectable change in substructure occurred, the consecutive curves obtained as a function of annealing time appeared as perfect mirror images of each other, since by means of the reversible motor the direction of the specimen rotation was reversed. Conversely, if changes in the substructure occurred the consecutive rocking curves exhibited corresponding modifications in shape. For the annealing of the specimens, which was carried out

(11) Y. Nakayama, S. Weissmann and T. Imura, Direct Observations of Imperfections in Crystals, p. 573, Interscience Publ., div. of John Wiley & Sons, New York, 1962.
(12) S. Weissmann, M. Hirabayashi and H. Fujita, J. Appl. Phys. 32, 1156 (1961).

on the x-ray unit without removal of the specimen, an elliptical reflector lamp was used.

It was found that low-angle boundaries perpendicular to the basal plane did not offer any appreciable resistance to a shearing force parallel to the basal plane if they were pure tilt boundaries, but constituted substantial barriers if they were asymmetrical, that is, made up of screw and edge dislocations. If the external force exceeded a critical value these asymmetrical, low-angle boundaries became sites where fracture occurred. The strengthening effect of the asymmetrical low-angle boundaries was attributed to the effective stress field of the screw dislocations, which were mechanically stabilized by the edge dislocations. The stress field of the screw dislocations was also responsible for the thermal instability of the asymmetrical low-angle boundaries, which on annealing were gradually converted into pure tilt boundaries. A coarse substructure established after annealing was thermally very stable. On solidification after partial melting of the crystal, the coarse substructure was re-established, whereas the fine substructure was entirely modified (12).

C. Structural Changes Associated with Recrystallization and Grain Growth (13)

Growth processes of 99.998% aluminum were studied by the combination method discussed in section 3. The recrystallized grains were shown to be the product of preferential subgrain growth whereby subgrains subtending large disorientation angles with respect to their neighbors exhibited the highest velocity of growth. The recrystallized grains emerging from the deformed matrix showed at first a high degree of lattice perfection. However, as growth proceeded lattice imperfections were incorporated into the growing grain and the lattice misorientation of the grain increased. These lattice imperfections arose either from grain impingement and adaptation to orientation differences which might have existed between the growing grain and the grain being consumed, or they might have been generated by overcoming barriers such as impurity-locked dislocations. The recrystallized grains exhibited occasionally a fine net of sub-boundaries which usually emanated from the advancing interface. In any case, the lattice defects were not survivals of defects introduced during the deformation process but were by-products of the growth process. However, owing to the large volume increase of the growing grain the number of dislocations per unit volume, that is to say, the dislocation density, steadily declined.

4. DIRECT OBSERVATION OF LATTICE DEFECTS IN CRYSTALS OF LOW DISLOCATION DENSITY BY X-RAY DIFFRACTION MICROSCOPY

In crystals of low dislocation density the direct observation of lattice defects by x-ray diffraction microscopy can be achieved in two different ways. One method is based on the effect of primary extinction contrast, while the other is based on the anomalous transmission effect of the x-ray beam.

4.1 X-Ray Diffraction Microscopy Based on Extinction Contrast

In highly perfect crystals contrast is governed by the effect of primary extinction. If a perfect crystal is set in reflecting position the energy of the

(13) S. Weissmann, Trans. ASM 53, 265 (1961).

incident, primary beam gets rapidly extinguished as the beam passes through the crystal, because the energy diverted into the secondary or reflected beam interacts intimately with the primary beam. One can see in a general way how this diminution may come about. The wave reflected by each crystal plane suffers a phase change of $\pi/2$ relative to that of the primary beam, so that the twice-reflected waves which again travel in the direction of the primary waves will have a phase difference of π relative to the primary waves. This phase difference results in a reduction of the amplitude of the primary beam. In a perfect crystal the definite phase relationship set up between the incident, the reflected and multiple-reflected waves leads to a constant interchange of energy between the primary and diffracted beams. The process results in a dynamic equilibrium which extinguishes the primary beam after penetrating to a depth of 0.1μ to 10μ for strong reflections and a larger distance for weaker reflections.

If a crystal contains a few dislocations the rupture of coherence in the perfect periodicity of the reflecting planes as well as the lattice strains associated with the dislocation lines decrease the primary extinction effect. The diffracted image of a lattice domain will, therefore, be enhanced in the vicinity of a dislocation line and this is the underlying reason why in nearly perfect crystals the dislocations can be made visible by x-ray diffraction microscopy.

The contrast, that is, the intensity above background I_D will depend on the direction of the lattice strain (Burgers vector b in the case of a dislocation) relative to the orientation of the reflecting (hkl) planes. The relation is given by

$$I_D = k(\vec{g} \cdot \vec{b}) \qquad (1)$$

where $\vec{g}$ = reciprocal lattice vector
$\vec{b}$ = displacement or strain vector (Burgers vector in case of a dislocation)
k = constant.

It will be seen that maximum contrast is achieved if the lattice strain is normal to the reflecting (hkl) planes and will be zero if it is parallel to them.

By applying the Berg-Barrett reflection method to crystals of LiF Newkirk (14) has successfully shown on the basis of extinction contrast individual dislocation lines and fine details of dislocation networks.

A refined variation of the Berg-Barrett method, the projection topography method of Lang, has found interesting application for the study of the dislocation structure in semiconducting crystals (15, 16, 17). The basic principle of this method is shown in Fig. 13. A collimated x-ray beam a impinges on a crystal b, which is so oriented and of such thickness as to permit the Bragg-reflected beam to pass in transmission. The diffracted beam is recorded on a fine-grained film c,

(14) J. B. Newkirk, Trans. Am. Inst. Min. & Metall. Engrs., 215, 483 (1959).
(15) A. R. Lang, J. Appl. Phys. 29, 527 (1958); 30, 1748 (1959).
(16) A. E. Jenkison and A. R. Lang, Direct Observation of Imperfections in Crystals, p. 471, Interscience Publ., div. John Wiley & Sons, New York (1962).
(17) G. H. Schwuttke, Direct Observation of Imperfections in Crystals, p. 497, Interscience Publ., div. John Wiley & Sons, New York (1962).

placed close to the crystal. Since the image of the specimen is larger than the width of the interposed slit, the specimen is moved synchronously with the film. A stationary screen d is provided which prevents the direct beam from striking the film.

Figure 14 shows a Lang camera commercially produced by the Rigaku-Denki Co. which is so designed that its greatest effectiveness is achieved when attached to a microfocussing x-ray source, preferably 10μ in size. Figure 15 illustrates an x-ray diffraction topograph of a silicon crystal produced by a Lang camera, disclosing clearly the pattern of the dislocation structure of the crystal.

X-ray topography is not only applicable to disclosure of the dislocation structure of crystals but is also capable of revealing segregation effects such as oxygen banding in silicon crystals (17). If the crystals to be analyzed contain, however, a large dislocation density, viz. larger than $10^6/cm^2$, or a large density of impurities, the x-ray topographs become so complicated that no unequivocal interpretation can be rendered and their usefulness becomes greatly reduced.

4.2 X-Ray Diffraction Microscopy Based on Anomalous Transmission Effects

An extensive review article on the anomalous transmission of x-rays has been published by Borrmann (18). The essential principles of this effect will be briefly outlined here. Anomalous transmission occurs only in nearly perfect crystals and consists of enhanced transmission of the direct beam if the crystal is held in diffracting position. When the crystal is rotated to any non-diffracting position the intensity of the transmitted direct beam is considerably reduced. This effect was discovered by Borrmann (19) and subsequently explained by Von Laue (20).

If a plane monochromatic x-ray wave enters a perfect crystal set for diffraction position, two standing waves are generated. The flow of energy takes place principally along the lattice planes and the direction of the standing waves is perpendicular to the flow direction. Taking the case of a simple lattice, one of these standing waves (A) may have its nodal planes coincide with the position of a family of (hkl) planes, while the other standing wave (N) has its nodes halfway between. If the crystal is assumed to consist of point absorbers taking the place of real atoms, the N wave will rapidly be absorbed due to its interactions with the point absorbers, while the A wave is transmitted with undiminished intensity through the crystal. Upon leaving the crystal the A wave splits into two equal components, namely, the transmitted beam R_o and the diffracted beam R (Figs. 16 and 17).

In the case of a real crystal consisting of scattering atoms whose scattering factor is known, the A wave has a finite absorption coefficient. The intensity of the x-ray beam emerging from the crystal will depend greatly on crystal perfection. Lattice defects destroying the periodicity of the crystal will reduce the intensity of the A wave, since the critical conditions necessary for the Borrmann (anomalous) transmission are being destroyed and normal absorption will then occur. Figure 16 shows schematically a simple experimental arrangement used by Schwuttke (21) to ob-

(18) G. Borrmann, Beitraege zur Physik und Chemie des 20 Jahrhunderts, edit. by Frisch, Paneth, Laves and Rosbaud, p. 262, Vieweg. Braunschweig, (1959).
(19) G. Borrmann, Z. Physik 42, 157 (1941); ibid. 127, 297 (1950).
(20) M. Von Laue, Acta Cryst. 2, 106 (1949).
(21) G. H. Schwuttke, J. Appl. Phys. 33, 2760 (1962).

tain anomalous transmission topographs of the dislocation structure of semiconducting crystals such as those shown in Fig. 17. In this picture the R and R_o images are completely identical, as expected from the theory of anomalous transmission. The dislocation lines are clearly visible as shadows because the anomalous transmitted wave field is not propagated in the strain field associated with the dislocations.

Segregation and precipitation of copper in silicon and arsenic in highly doped germanium crystals could also be disclosed by this method (21).

4.3 Comparison of Extinction and Anomalous Transmission Methods

The results obtained by the two methods are virtually identical. While both methods are restricted to the study of lattice defects of nearly perfect crystals, the conditions of obtaining maximum contrast of the image differ greatly. For best contrast the anomalous transmission method requires that the product of $\mu \times t \geqq 20$, while for the extinction method $\mu \times t \leqq 1$, where μ is the linear mass absorption coefficient and t (cm) is the thickness of the specimen. As a direct consequence of this condition soft radiation, viz. copper or cobalt, is used for the anomalous transmission method and penetrating radiation, viz. silver or molybdenum, for the extinction method if applied in transmission (Lang method).

The contrast images of lattice defects differ also in both methods. In the anomalous transmission method defects show up by absorption contrast, whereas in the extinction method the contrast is produced by enhancement of the transmitted intensity. If equal areas are recorded, the scanning extinction method requires approximately one half the exposure time necessary for the stationary anomalous transmission method (21).

5. DETERMINATION OF SUBSTRUCTURE CHARACTERISTICS BY IMAGE TRACING

A method has been recently developed by Weissmann, Gorman and Zwell (22) by which the substructure characteristics and dislocation densities of crystalline materials can be rapidly determined. The method is based on spatial tracing of reflection images and their extrapolation onto the specimen surface, using the method of least squares.

If a Bragg reflection is photographically recorded at increasing specimen-to-film distance, the parametric equations of the reflected ray are given by

$$\begin{aligned} x &= x_o + \beta_x h \\ y &= y_o + \beta_y h \end{aligned} \qquad (1)$$

where (x_o, y_o), (x, y) are the coordinates of the reflection images on the crystal surface and on the film, respectively, h is the specimen-to-film distance and (β_x, β_y) are the slope parameters. From measurements of the coordinates x_i, y_i corresponding to the distances h_i, the x_o, y_o coordinates on the specimen surface are determined by the method of least squares, using the equations (22)

(22) S. Weissmann, L. A. Gorman and L. Zwell, J. Appl. Phys. 33, 3131 (1962).

$$x_o = \frac{\Sigma x \Sigma h^2 - \Sigma h \Sigma hx}{n\Sigma h^2 - (\Sigma h)^2}$$

$$y_o = \frac{\Sigma y \Sigma h^2 - \Sigma h \Sigma hy}{n\Sigma h^2 - (\Sigma h)^2} \qquad (2)$$

Similarly, the slope parameters are determined by the method of least squares from the expressions

$$\beta_x = \frac{n\Sigma hx - \Sigma h \Sigma x}{n\Sigma h^2 - (\Sigma h)^2}$$

$$\beta_y = \frac{n\Sigma hy - \Sigma h \Sigma y}{n\Sigma h^2 - (\Sigma h)^2} \qquad (3)$$

Referring to Fig. 18, the size of the images is measured in terms of Δy and Δx for various values of h, and the dimensions on the specimen, Δx_o and Δy_o, are determined by the application of Eq. (2).

If a parallel, crystal-monochromatized radiation is used the change of the size parameters Δy and Δx for various h values gives information about the vertical lattice misalignment, $\Delta\beta_y$, and the horizontal lattice misalignment $\Delta\beta_x$. These can be computed with the aid of Eq. (3).

The disorientation angle between subgrains can be computed from the measurements of the vertical separation, Δt, and the horizontal separation, Δs, of the images as a function of h and substituting these values in Eq. (3).

For this method the requirements of instrumentation are reduced to a minimum. Its application should be within the reach of any laboratory having standard diffraction equipment.

ACKNOWLEDGMENT

Thanks are due to Dr. G. H. Schwuttke for his generous contribution of Figs. 15, 16 and 17.

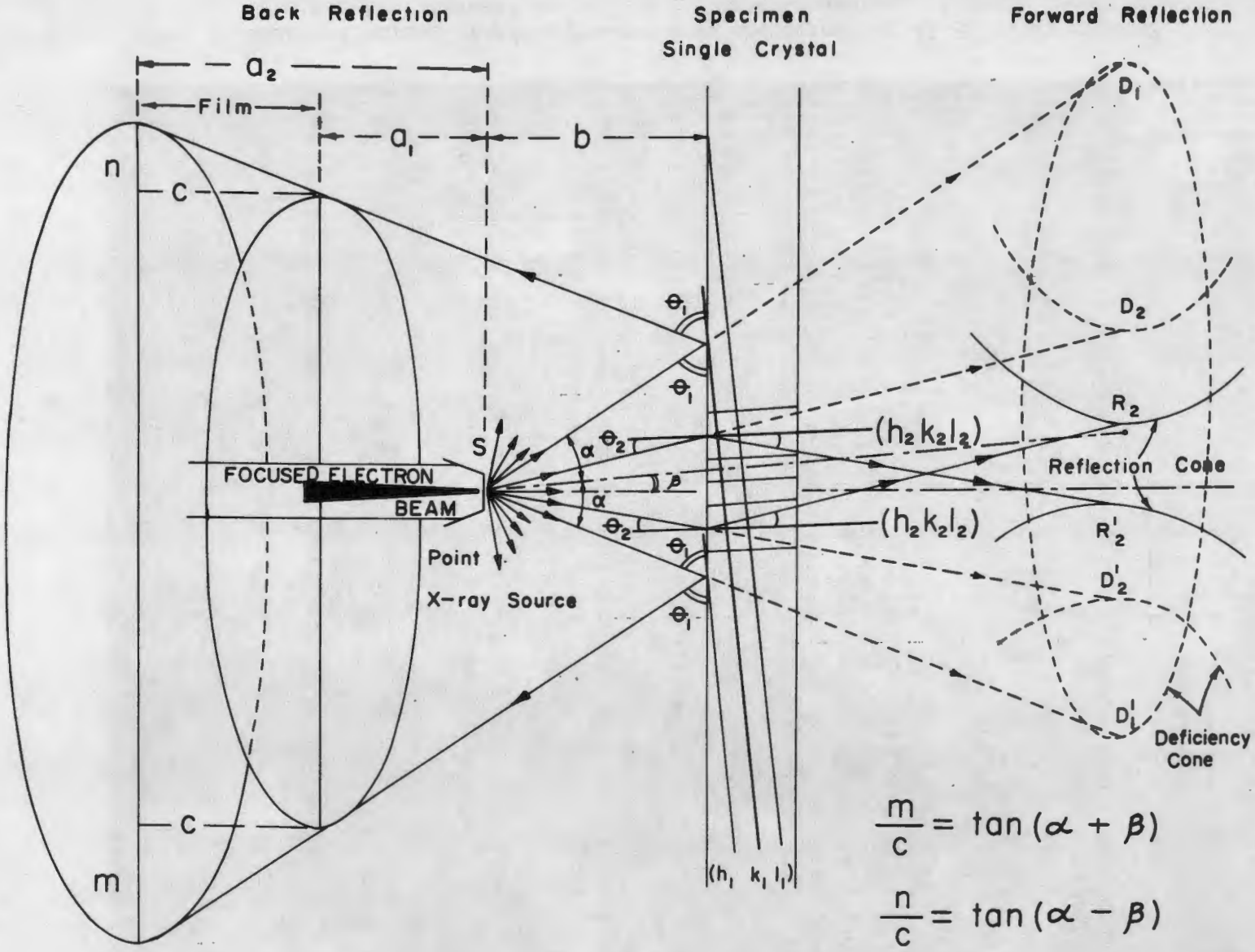

Fig. 1--Schematic representation of the generation of pseudo-Kossel patterns by the divergent beam method.

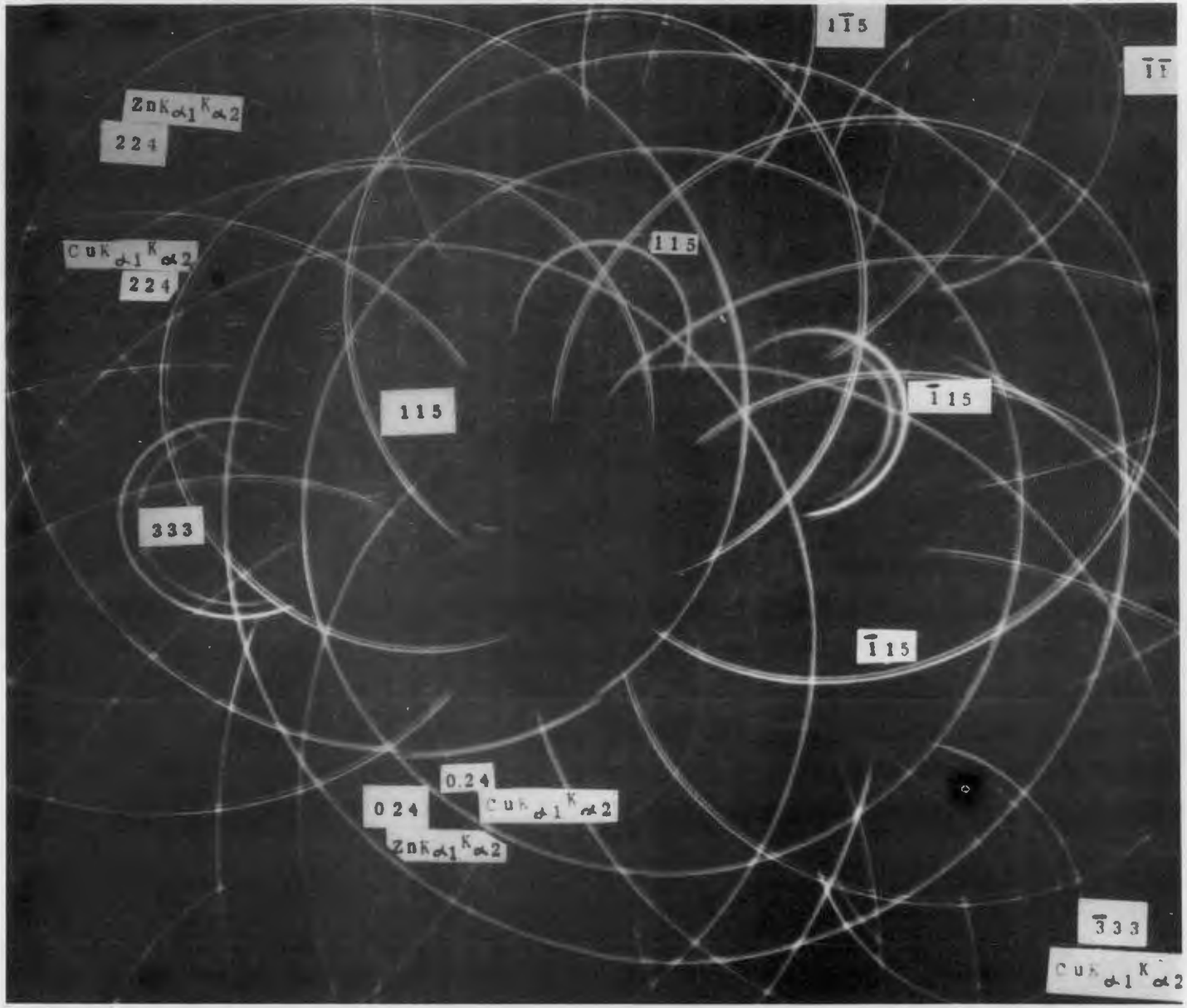

Fig. 2--Back-reflection divergent x-ray beam photograph of Al-3.85% Cu crystal. Solution heat-treated at 540° C and water-quenched. A brass target was employed, giving rise to sets of CuK_α and ZnK_α lines.

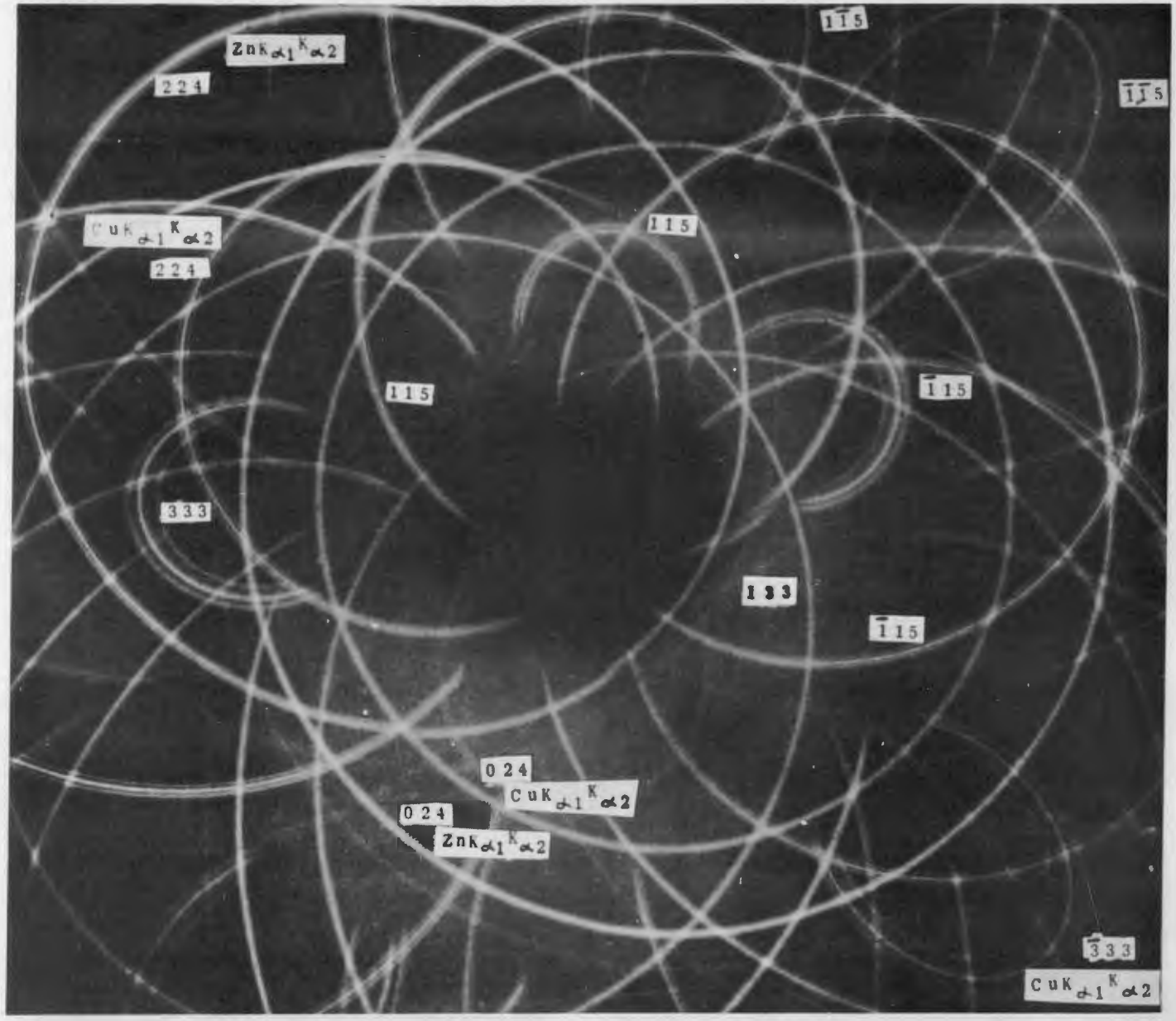

Fig. 3--Superposition of two back-reflection divergent x-ray beam photographs of Al-3.85% Cu crystal, as quenched and aged at 320° C for 1/2 hour, illustrating anisotropic lattice expansion induced by age-hardening.

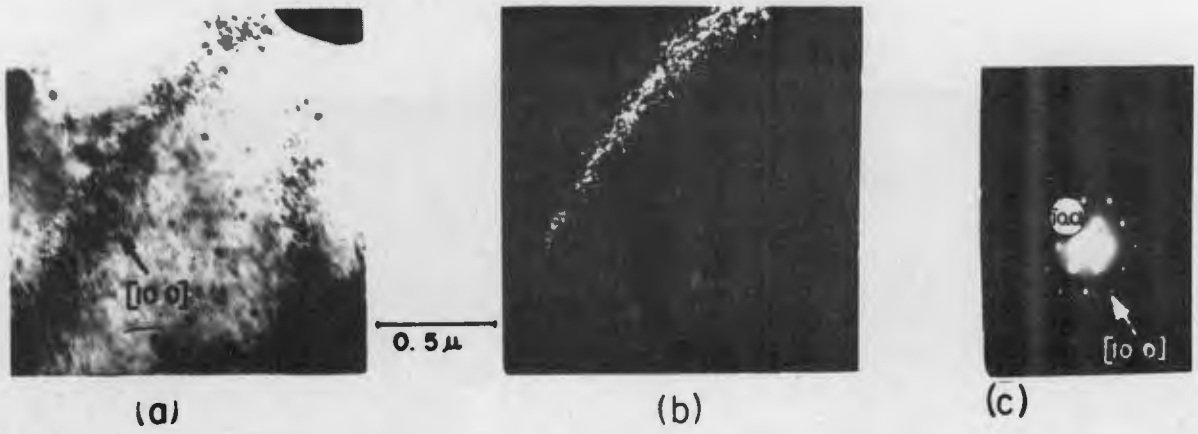

Fig. 4--Transmission electron micrograph of z-cut quartz crystal irradiated 1×10^{19} nvt. (a) Bright field. (b) Dark field. (c) Selected area diffraction. Dark field taken from (10.0) reflection.

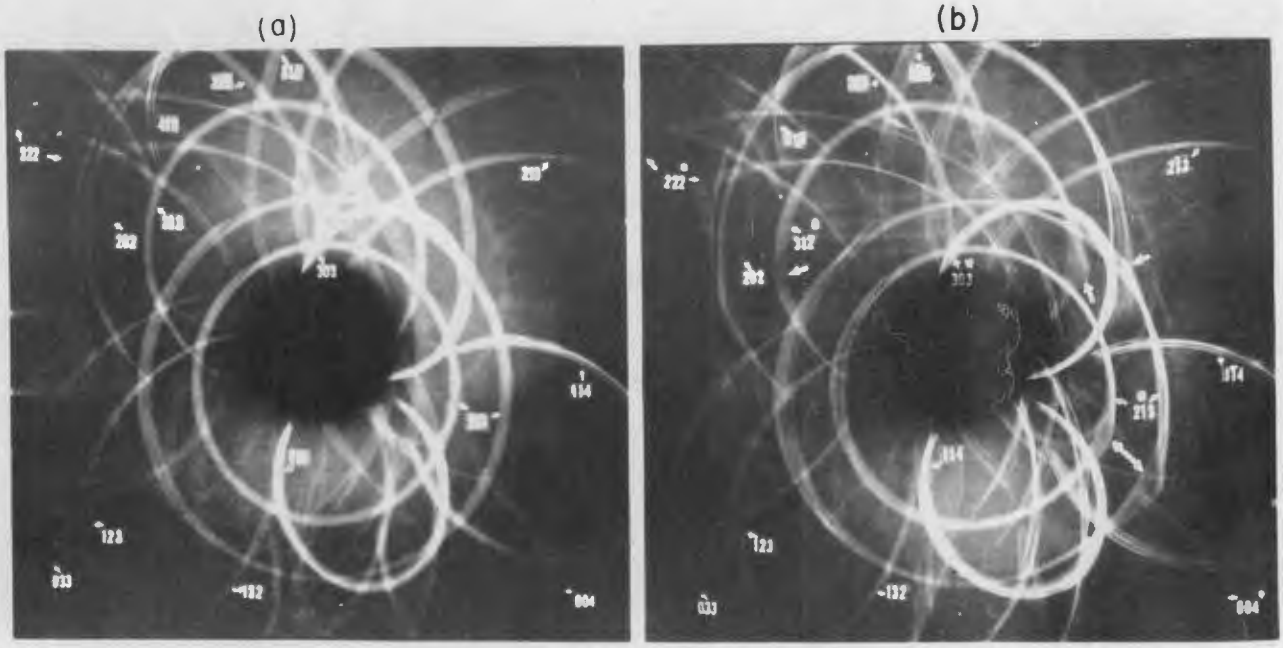

Fig. 5--Back-reflection x-ray divergent beam photographs of Mo crystal. a) Undeformed. b) Deformed 5.8% at room temperature. Note: Irradiation of adjacent lattice domains by multiple exposure technique. Distorted lattice domains indicated by arrows.

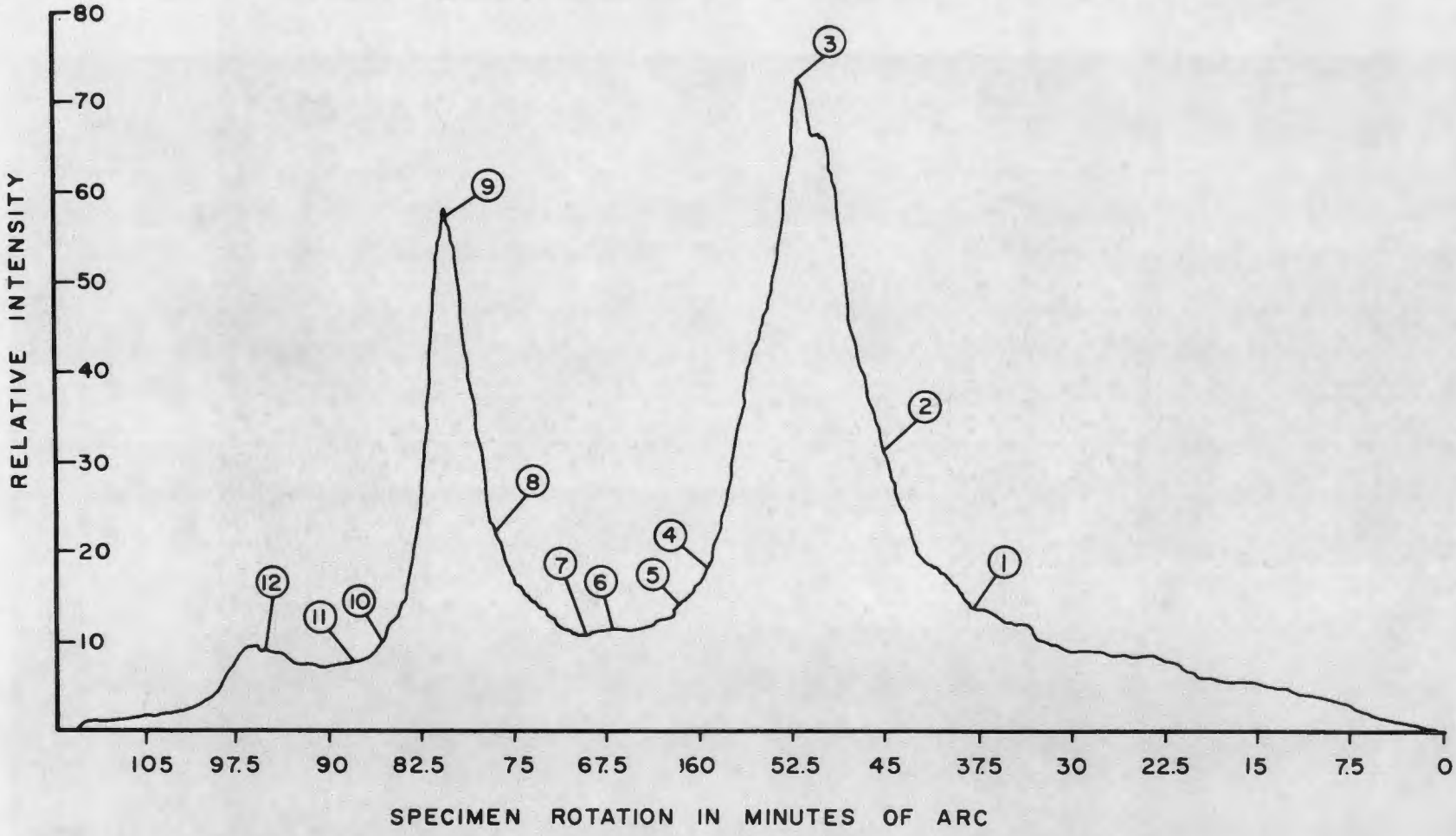

Fig. 6--Reflection curve of magnesium single crystal as obtained by the double-crystal diffractometer method. $CuK_{\alpha 1}$ radiation. (1, -1) position.

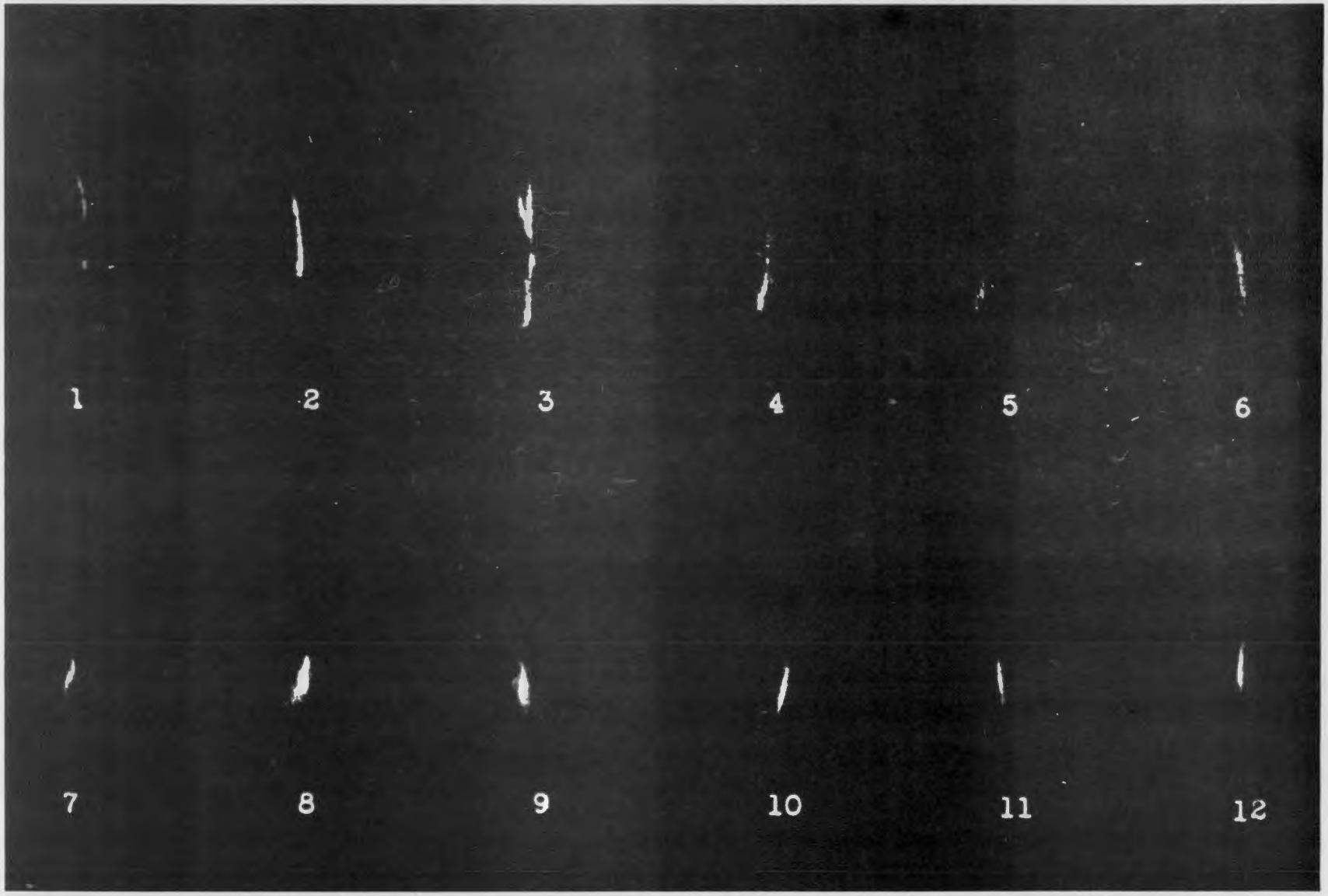

Fig. 7--Reflection images of magnesium crystal taken in front of radiation counter. The numbers refer to the corresponding discrete rotation positions of the specimen shown in Fig. 6

Fig. 8--Detailed view of (422) reflection of multiple-exposure diagram exhibiting multi-modal intensity distribution curves typical of subgrain structure. Al 99.95% pure, 96% reduced and annealed 1 hour at 300° C. Specimen rotation interval 4'.

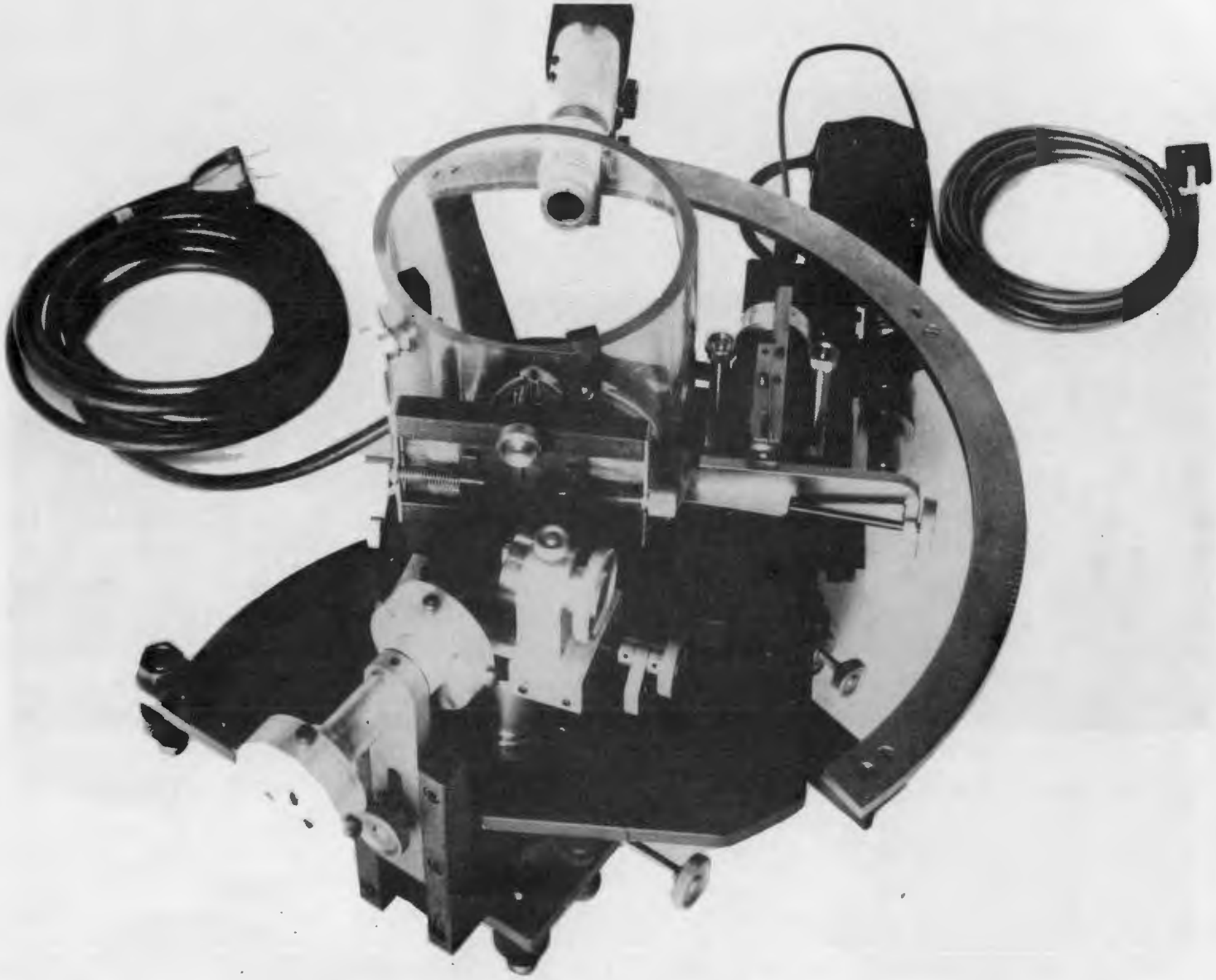

Fig. 9--X-ray double-crystal diffractometer. Experimental arrangement for use of crystal-monochromatized radiation.

Fig. 10—X-ray oscillation reflection micrograph of tungsten single crystal grown by arc fusion. Effective focal spot size 40μ. Disclosure of macroscopic and microscopic substructure. Magnification 40 x.

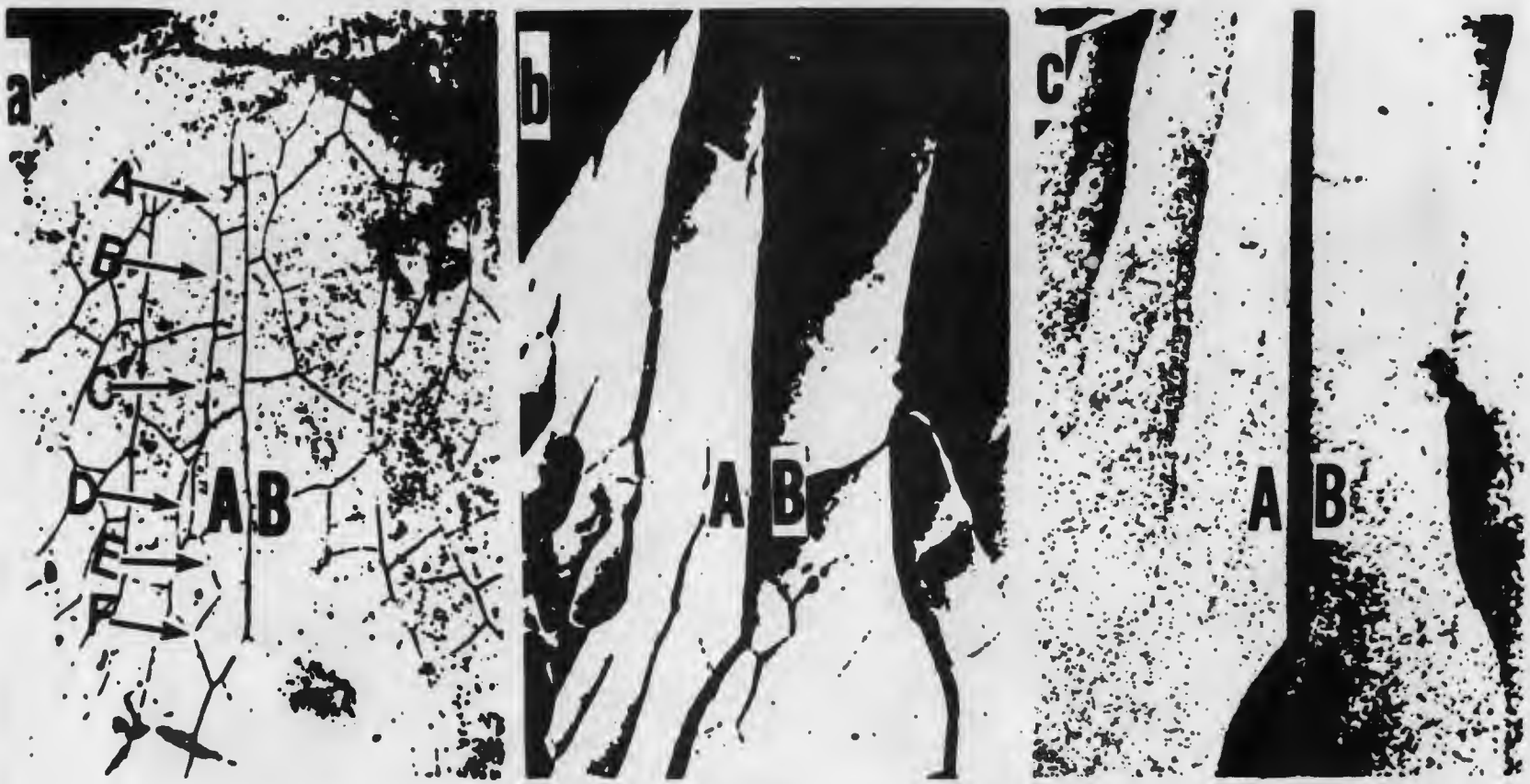

Fig. 11--Correlation of substructure in tungsten crystal (18.5x). a) Light micrograph of substructure disclosed by etching with 3% boiling H_2O_2. b) X-ray rotation reflection micrograph. Unfiltered radiation, Cu target. Effective size of focal spot, 40 μ. c) X-ray rotation reflection micrograph. Unfiltered radiation with superimposed crystal-monochromatized $CuK_{\alpha 1}$ radiation.

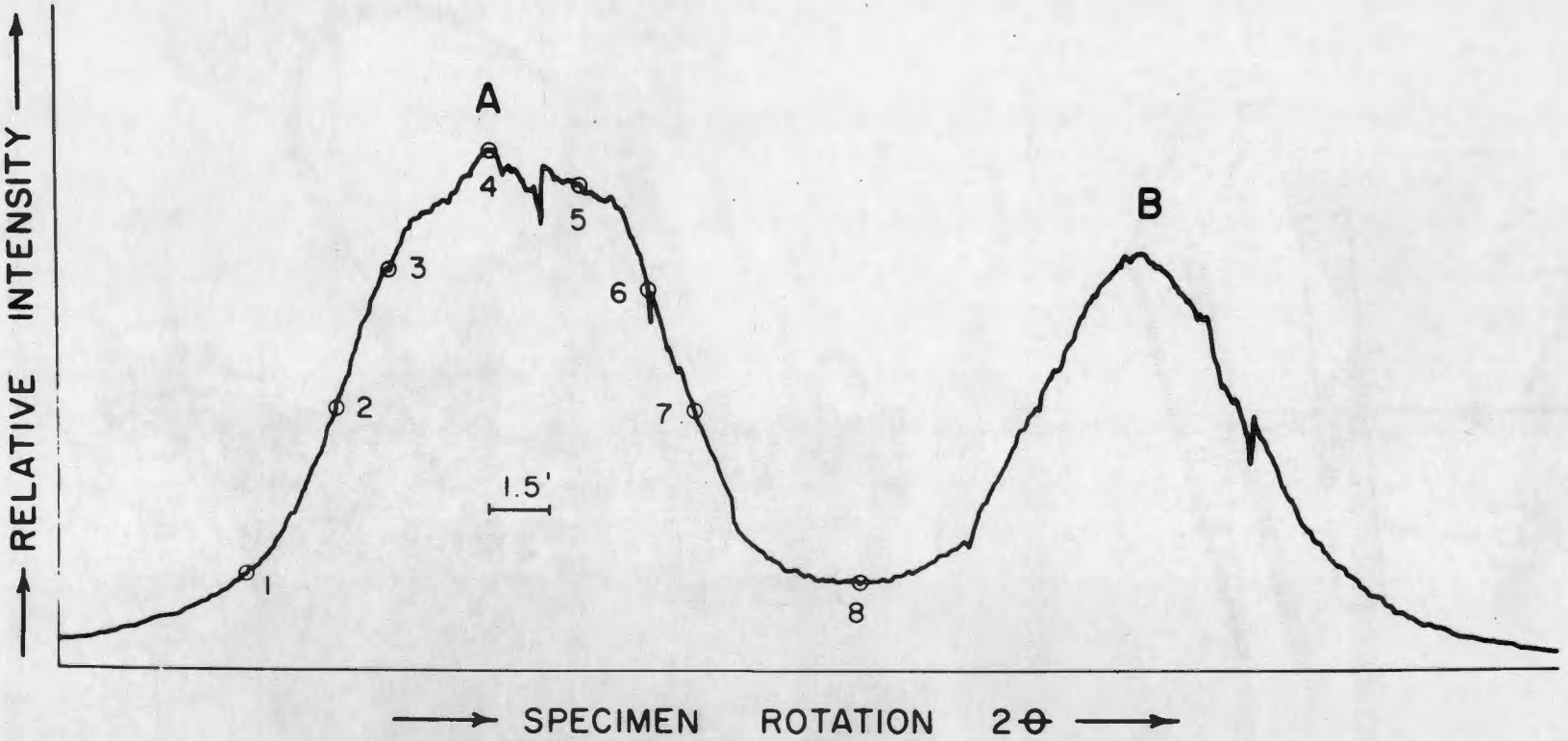

Fig. 12--Double-crystal diffractometer curve of macroscopic subgrains A and B of Figs. 10 and 11.

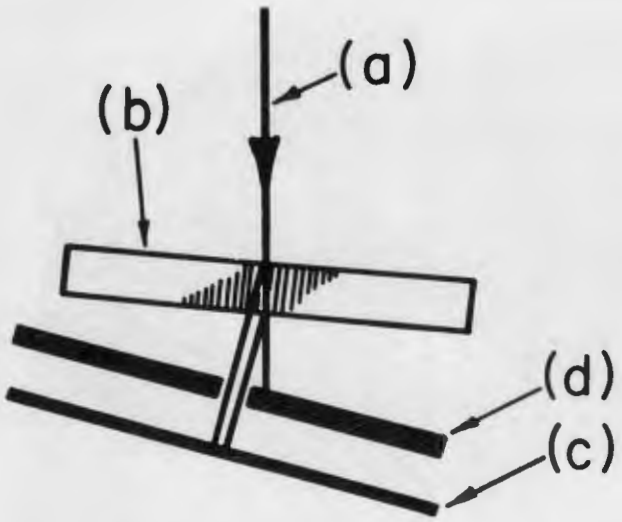

Fig. 13--Principle of Lang's x-ray projection topography. (a) Collimated x-ray beam. (b) Crystal. (c) Film. (d) Stationary screen.

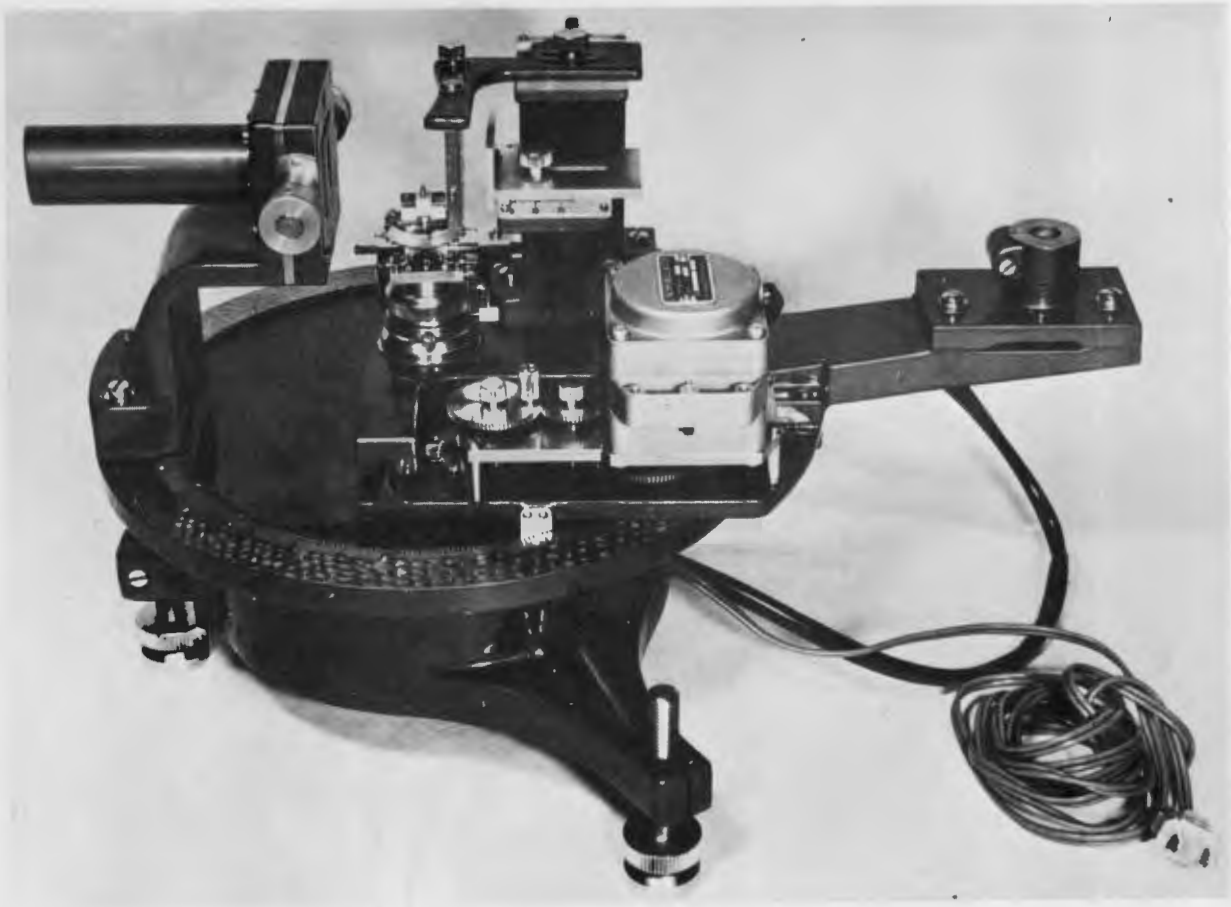

Fig. 14--Commercial Lang camera for x-ray diffraction topography (courtesy of Rigaku-Denki Co.).

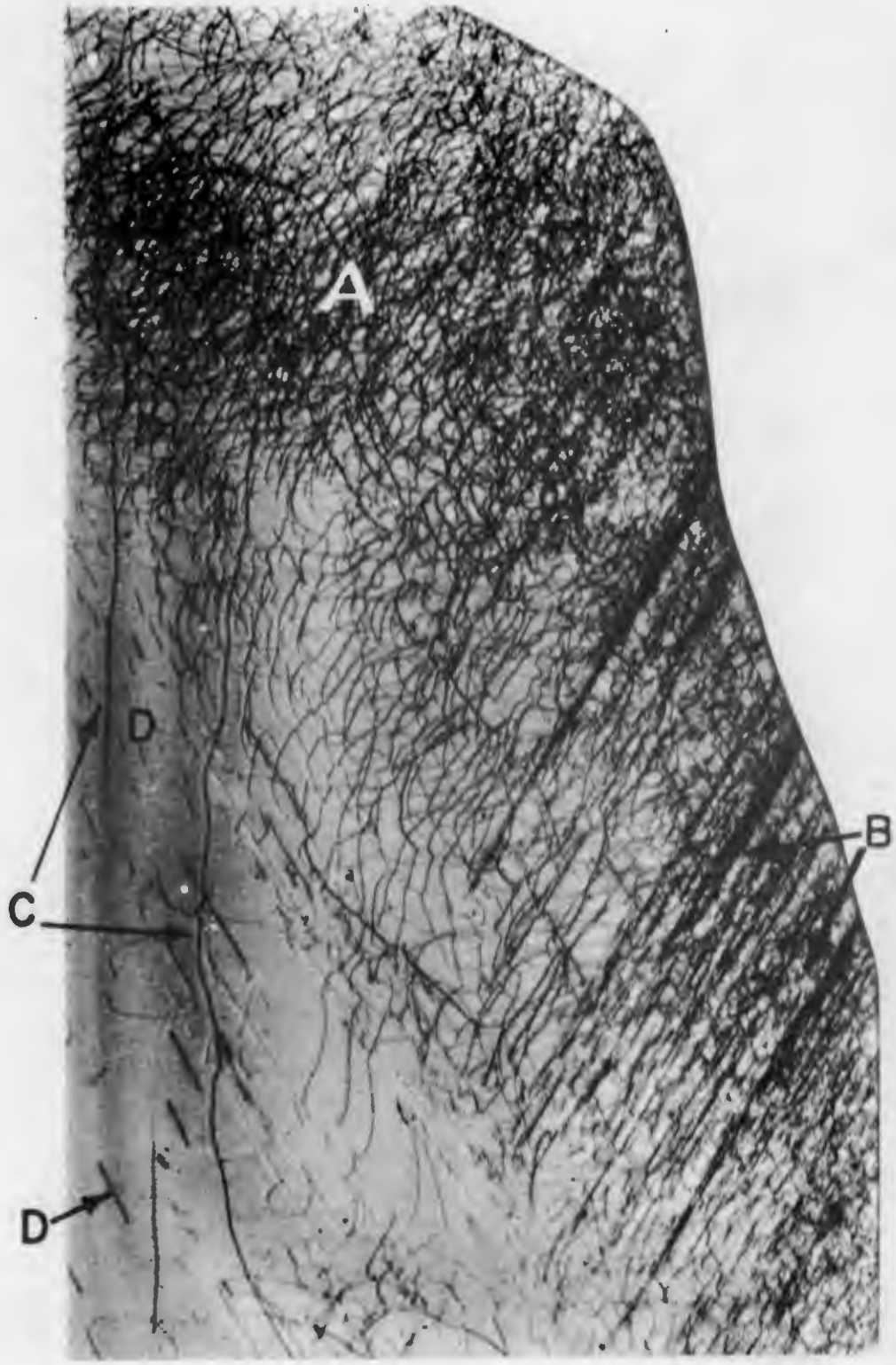

Fig. 15—X-ray diffraction topograph of silicon (220 reflection). Growth axis ⟨111⟩ (courtesy of G. H. Schwuttke). The dislocation density at A is approximately 10^5 lines/cm^2. Alignment of edge dislocations at D. Long dislocation lines with maximum contrast at C. The short lines at D have 60° Burgers vector lying in the plane perpendicular to (110).

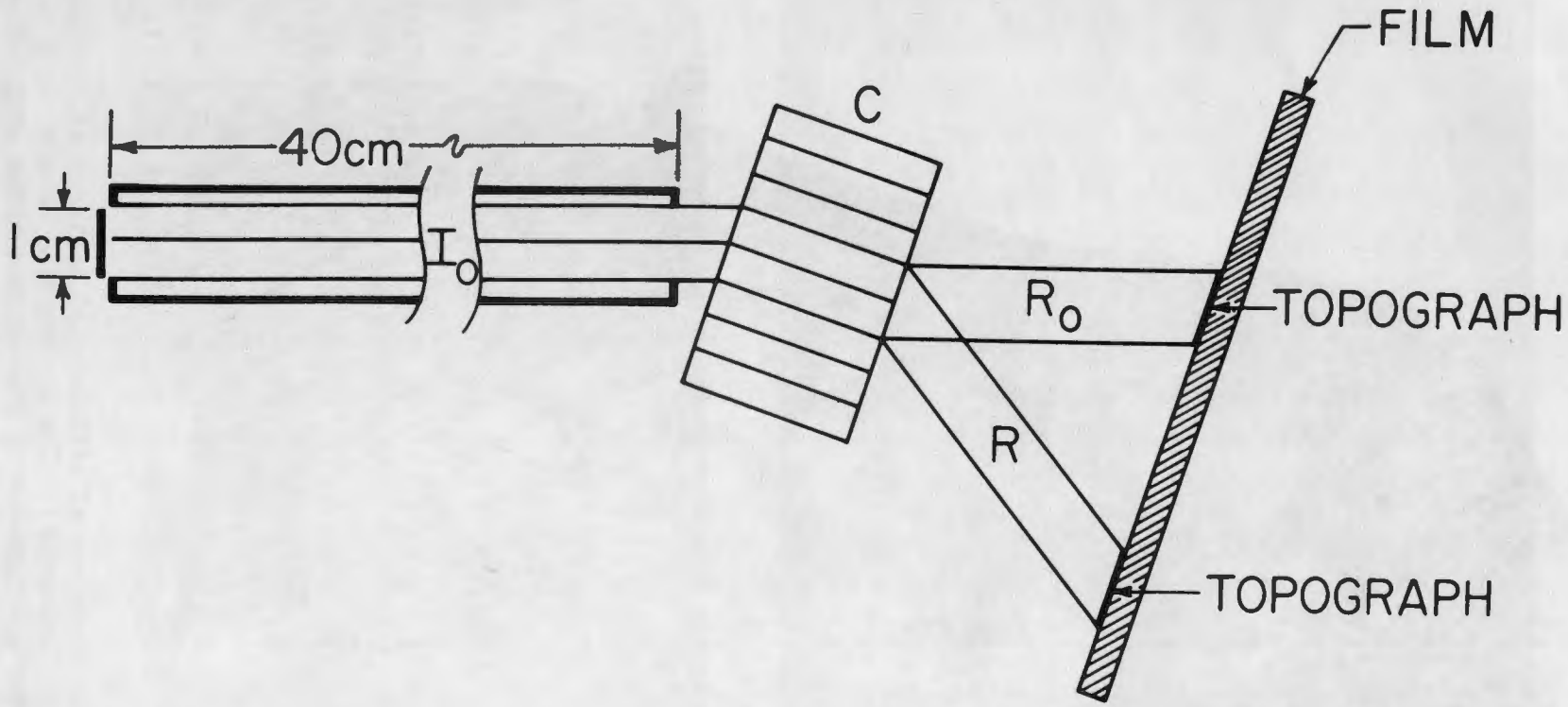

Fig. 16—Sketch of experimental arrangement for the anomalous transmission method (after Schwuttke[21]).

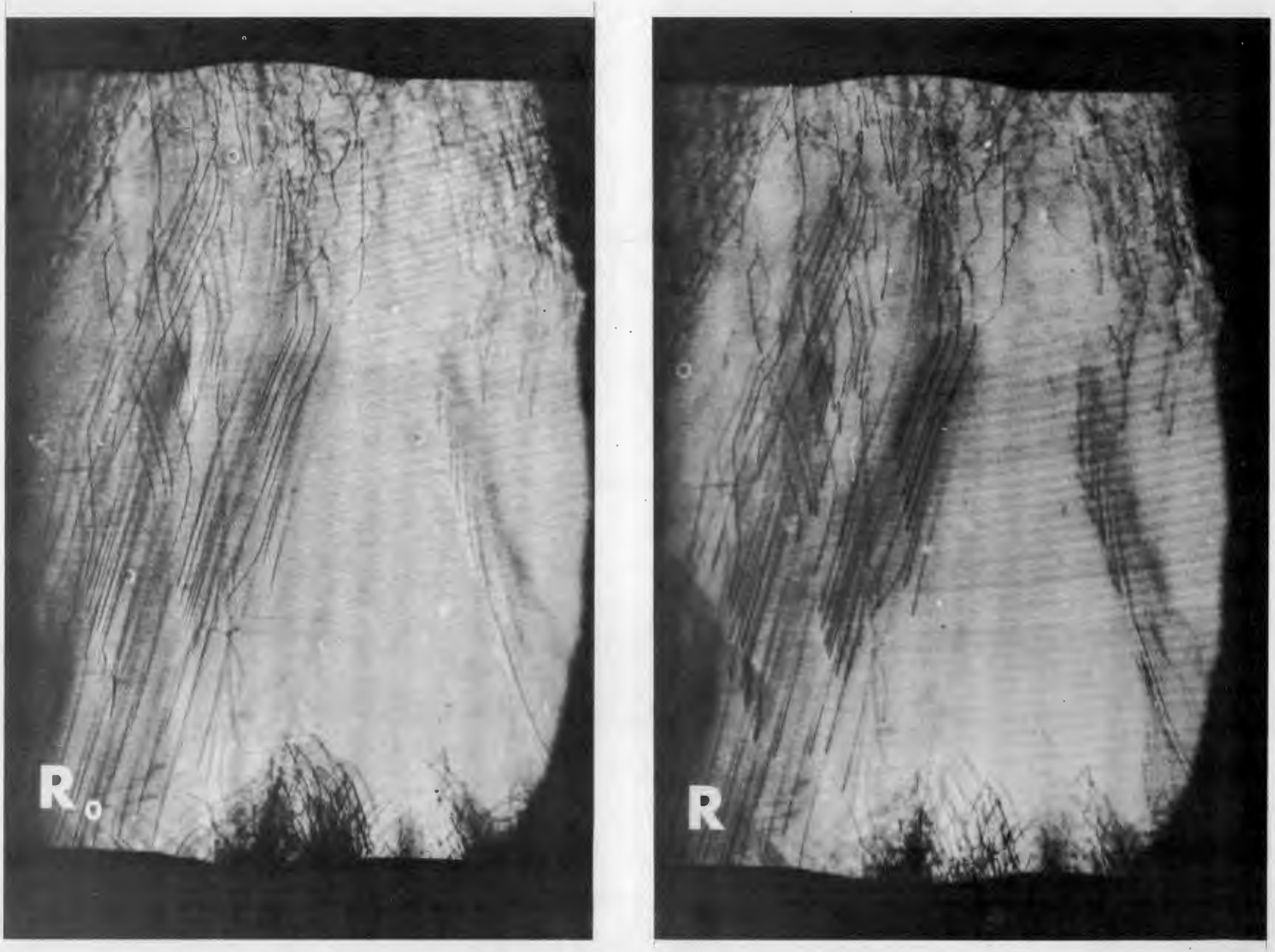

Fig. 17--R and R_o image of germanium wafer showing dislocations and segregation of arsenic. (220) reflection. 12 x. (After Schwuttke[21]).

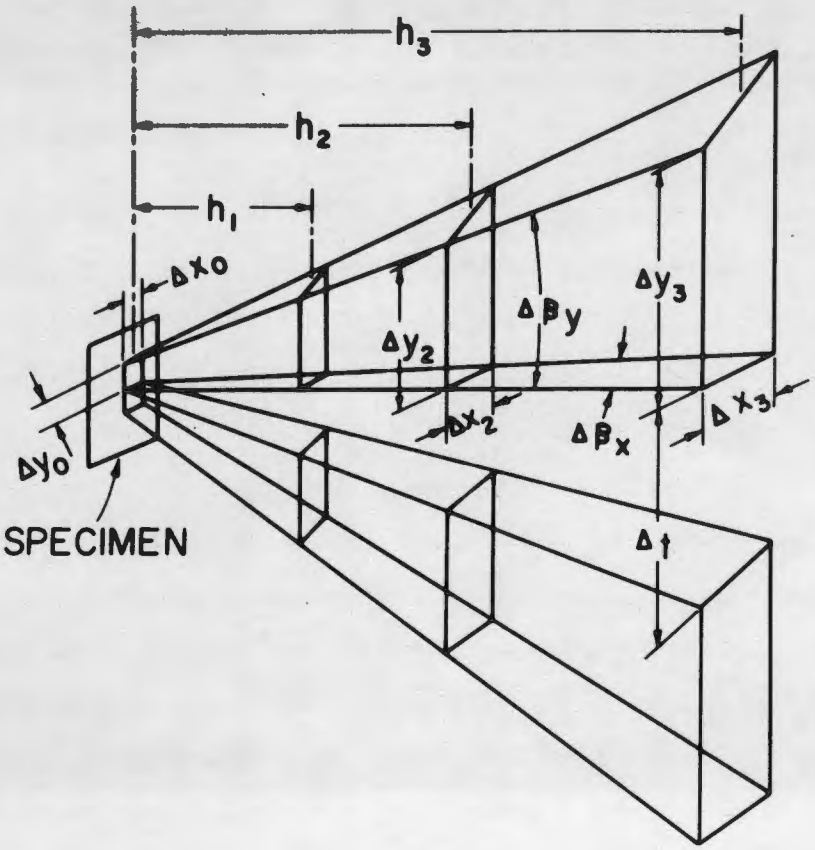

Fig. 18--Schematic representation of spatial image tracing showing dependence of image size and separation on substructure characteristics.